J Mater Sci (2009) 44:4860–4873
DOI 10.1007/s10853-009-3742-y

# Simultaneously enhanced tensile and compressive response of AZ31–Nano$Al_2O_3$–AA5052 macrocomposite

**M. Paramsothy · S. F. Hassan · N. Srikanth · M. Gupta**

Received: 5 January 2009 / Accepted: 10 July 2009 / Published online: 24 July 2009


**Abstract** New bimetal AZ31–$Al_2O_3$/AA5052 macrocomposite comprising (a) $Al_2O_3$ nanoparticle-reinforced magnesium alloy AZ31 shell and (b) aluminum alloy AA5052 millimeter-scale core reinforcement was fabricated using solidification processing followed by hot coextrusion. Microstructural characterization revealed more rounded intermetallic particle of decreased size, reasonable $Al_2O_3$ nanoparticle distribution, and non-dominant (0 0 0 2) texture in the longitudinal and transverse directions in the AZ31–$Al_2O_3$ nanocomposite shell. Interdiffusion of Mg and Al across the core–shell macrointerface into each other was also significant. Compared to monolithic AZ31, the AZ31–$Al_2O_3$ shell exhibited significantly higher hardness (+33%). In tension, the presence of $Al_2O_3$ nanoparticles (in the AZ31 shell) and AA5052 core significantly increased stiffness (+39%), yield strength (0.2% TYS) (+9%), ultimate strength (UTS) (+19%), average failure strain (+7%), and work of fracture (WOF) (+27%) of AZ31. In compression, the presence of $Al_2O_3$ nanoparticles (in the AZ31 shell) and AA5052 core significantly increased yield strength (0.2% CYS) (+58%), ultimate strength (UCS) (+4%), average failure strain (+11%), and WOF (+49%) of AZ31. The effect of joint presence of (a) $Al_2O_3$ nanoparticles (in the AZ31 shell) and (b) AA5052 millimeter-scale core on tensile and compressive properties of AZ31 is investigated in this article.

M. Paramsothy · M. Gupta (✉)
Department of Mechanical Engineering, National University of Singapore, 9 Engineering Drive 1, 117576 Singapore, Singapore
e-mail: mpegm@nus.edu.sg

S. F. Hassan
Department of Mechanical Engineering, King Fahd University of Petroleum & Minerals, P.O. Box No. 1061, Dhahran 31261, Kingdom of Saudi Arabia

N. Srikanth
Department of Industrial & Systems Engineering, Centre for Management of Science and Technology, National University of Singapore, 7 Engineering Drive 1, 117574 Singapore, Singapore

## Introduction

Magnesium and aluminum are commonly used light metals in weight-critical automotive and aerospace structural applications. Mg is about 35% lighter than Al with consequent superior damping characteristics, and both have similar melting points and strengths. However, the ductility of Mg is limited compared to Al. This can be attributed to limited number of active (basal) slip systems in its HCP structure. Also, Mg has a lower elastic modulus (40–45 GPa) than Al (69.6 GPa) [1]. Traditional alloying can be used to increase the strength and ductility of Mg [2]. Additionally, based on the use of discontinuous reinforcement, many properties of Mg have been improved beyond the limits of alloying [3]. In recent years, three methods that have been tried to improve the strength, ductility, and modulus of Mg are (a) use of various oxide nanoparticles as well as CNTs for improving strength and ductility [4–6], (b) use of metallic particles such as Ti and Mo for improving ductility [7–9], and (c) use of micron size ceramic particulates for improving strength and modulus [10, 11]. AZ31 is a very commonly used Al-containing (or Zr-free) Mg alloy in the world today. It is characterized by (a) low cost, (b) ease of handling, and (c) good strength and ductility. Recently, AZ31 has been surface reinforced with SiC microparticulates [12], $C_{60}$ molecules [13], and multi-walled carbon nanotubes [14], using the friction stir

processing technique. Here, good dispersion and hardening of the base matrix were reported. Similar findings along with grain refinement were also reported for AZ31 reinforced with SiC and $B_4C$ microparticulates using gas–tungsten arc with simultaneous reinforcement powder feeding processing technique [15–17]. In the AZ31/SiC microcomposite, defect-free and adherent particle–matrix interface has been reported [16, 17]. Pulsed current hot pressing has been used to incorporate TiNi shape memory alloy fibers in AZ31 matrix without significant interfacial reaction [18]. As a consequence of residual compressive stress in the AZ31 matrix due to phase change-induced shrinkage of the TiNi fiber, the yield stress and elongation in the AZ31/TiNi microcomposite increased with temperature (strength significantly exceeded that of AZ31 matrix). Recently, researchers added $Al_2O_3$ nanoparticles to AZ31 using disintegrated melt deposition (DMD). Here, the tensile ductility and strength of AZ31 were significantly increased and compromised [19]. Regarding millimeter-length scale integration of bimetals including bimetal rolling of cladded sheet and extrusion of cladded rod, limited studies have been done involving the Mg–Al [20–24], Al–Cu [25–29], Cu–steel [26–29], Al–steel [30, 31], brass–steel [32], Al–Zn [33], Al–Sn [33], Al–Pb [33, 34], and Ni–Ti [35] bimetal material systems. The existence of stressed bimetal interface is suggested by some of the findings in these studies. The results of literature search indicate that no attempt has been made to simultaneously improve the stiffness, strength, and ductility of AZ31 magnesium alloy via (1) addition of $Al_2O_3$ or any other nanoparticles followed by (2) integration with AA5052 or any other aluminum alloy in millimeter-length scale, using a lower cost solidification processing methodology.

Accordingly, one of the primary aims of this study was to simultaneously increase stiffness, strength, and ductility of AZ31 by (1) addition of $Al_2O_3$ nanoparticles followed by (2) integration with AA5052 aluminum alloy in millimeter-length scale. Another aim of this study was to evaluate the compressive properties of AZ31–$Al_2O_3$/AA5052 bimetal macrocomposite considering end applications requiring compressive loading. The AZ31–$Al_2O_3$/AA5052 bimetal macrocomposite was formed using combination of DMD method [36, 37] and top-pouring followed by hot coextrusion.

## Experimental procedures

### Materials

In this study, AZ31 rod (2.50–3.50 wt%Al, 0.60–1.40 wt%Zn, 0.15–0.40 wt%Mn, 0.10 wt%Si, 0.05 wt%Cu, 0.01 wt%Fe, 0.01 wt%Ni, balance Mg, supplied by Alfa Aesar, MA, USA) was used as shell matrix material. $Al_2O_3$ nanoparticles (50 nm size) supplied by Baikowski (Japan) were used as the reinforcement phase for the AZ31 shell. AA5052 sheet (nominally 2.2–2.8 wt%Mg, 0.25 wt%Si, 0.40 wt%Fe, 0.10 wt%Cu, 0.10 wt%Mn, 0.15–0.35 wt%Cr, 0.10 wt%Zn, 0.15wt% others, balance Al, supplied by Yan San Metals Pte Ltd., Singapore) was used as the millimeter-scale core reinforcement phase. AZ31 rod and AA5052 sheet were sectioned to smaller pieces. All oxide and scale surfaces were removed using machining. All surfaces were washed with ethanol after machining.

### Primary processing

Monolithic AZ31 was cast using the DMD method [36, 37]. This involved heating the AZ31 rod to 750 °C in an inert Ar gas atmosphere in a graphite crucible using a resistance heating furnace. The crucible was equipped with an arrangement for bottom pouring. Upon reaching the superheat temperature, the molten slurry was stirred for 3 min at 460 rpm using a twin blade (pitch 45°) mild steel impeller to facilitate the uniform distribution of heat. The impeller was coated with Zirtex 25 (86%$ZrO_2$, 8.8%$Y_2O_3$, 3.6%$SiO_2$, 1.2%$K_2O$ and $Na_2O$, and 0.3% trace inorganics) to avoid iron contamination of the molten metal. The melt was then released through a 10-mm diameter orifice at the base of the crucible. The melt was disintegrated by two jets of argon gas oriented normal to the melt stream and located 265 mm from the melt pouring point. The argon gas flow rate was maintained at 25 lpm. The disintegrated melt slurry was subsequently deposited onto a metallic substrate located 500 mm from the disintegration point. An ingot of 40 mm diameter was obtained following the deposition stage. To form the AZ31–1.5 vol.%$Al_2O_3$ nanocomposite (see Fig. 1), $Al_2O_3$ nanoparticle powder was isolated by wrapping in Al foil of minimal weight (<0.50 wt% with

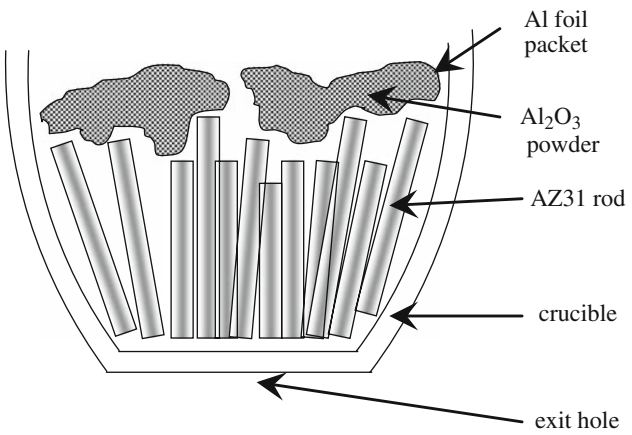


**Fig. 1** Arrangement of raw materials in crucible before casting, in obtaining AZ31–1.5 vol.%$Al_2O_3$ nanocomposite shell material

respect to AZ31 matrix weight) and arranged on top of the bundle of AZ31 sections, with all other DMD parameters unchanged. All monolithic and nanocomposite ingots were sectioned into billets. To form the macrocomposite, a single cavity of predetermined diameter was machined centrally into the 40-mm diameter AZ31–1.5 vol.%$Al_2O_3$ nanocomposite billet, the central cavity was screw tapped (depth, width, and angle of thread were 0.75 and 0.87 mm, and 60°, respectively), and AA5052 was top-poured (at 800 °C) to fill the threaded cavity. Screw tapping of the central cavity in the macrocomposite billet was done to increase the consistency of material flow during hot coextrusion.

### Secondary processing

The monolithic and macrocomposite billets were machined to 36-mm diameter and hot extruded using 20.25:1 extrusion ratio on a 150 ton hydraulic press. The extrusion temperature was 350 °C. The billets were held at 400 °C for 60 min in a furnace prior to extrusion. Colloidal graphite was used as a lubricant. Rods of 8 mm were obtained.

### Quantitative assessment of AA5052

The AA5052 volume fraction of the as-solidified macrocomposite billet was obtained by computing the volume of the threaded cavity using distilled water as fluid and dividing subsequently by the total volume of the 36-mm diameter billet.

### Microstructural characterization

Microstructural characterization studies were conducted on metallographically polished monolithic and macrocomposite extruded samples to determine (a) grain size, (b) intermetallic particle characteristics (type, size, and roundness ratio), (c) $Al_2O_3$ nanoparticle reinforcement distribution, (d) interfacial integrity (debonding presence as well as intermetallic particle presence and type), and (e) AZ31 texture (in the longitudinal and transverse directions). Olympus metallographic microscope was used for observing AZ31-based grains and related intermetallic particles. Hitachi S4300 field-emission scanning electron microscope (FESEM) was used for observing AA5052 grains and related intermetallic particles, $Al_2O_3$ nanoparticle reinforcement distribution, as well as AZ31–1.5 vol.%$Al_2O_3$–AA5052 interfacial integrity. Image analysis using Scion software was carried out to determine grain size. Intermetallic particle type was determined using energy dispersive X-ray spectroscopy (EDS). For intermetallic particles not located at the interface, X-ray diffraction (XRD) studies were also carried out to determine the particle type based on lattice spacing ($d$) match with corresponding standard values. XRD studies were conducted using $CuK_\alpha$ radiation ($\lambda = 1.5406$ Å) with a scan speed of 2°/min in an automated Shimadzu LAB-X XRD-6000 diffractometer. For intermetallic particles not located at the interface, image analysis using Scion software was carried out to determine intermetallic particle size and roundness ratio. XRD studies were conducted to also determine the dominant textures of AZ31 in the transverse and longitudinal (extrusion) directions.

### Hardness

Microhardness measurements were made on polished monolithic and macrocomposite extruded samples. Vickers microhardness was measured using Matsuzawa MXT50 automatic digital microhardness tester using 25 gf indenting load.

### Tensile testing

Smooth bar tensile properties of the monolithic and macrocomposite extruded samples were determined based on ASTM E8M-05. Round tension test samples of 5-mm diameter and 25-mm gauge length were subjected to tension using an MTS 810 machine equipped with an axial extensometer with a crosshead speed set at 0.254 mm/min. Fractography was performed on the tensile fracture surfaces using Hitachi S4300 FESEM.

### Compressive testing

Compressive properties of the monolithic and macrocomposite extruded samples were determined based on ASTM E9-89a. Samples of 8-mm length ($l$) and 8-mm diameter ($d$) where $l/d = 1$ were subjected to compression using an MTS 810 machine with 0.005 $min^{-1}$ strain rate. Compressive force was applied parallel to the extrusion direction. Fractography was performed on the compressive fracture surfaces using Hitachi S4300 FESEM.

## Results

### Macrostructural characteristics

No macrostructural defects were observed for extruded rods of monolithic AZ31 and AZ31–1.5 vol.%$Al_2O_3$/AA5052 macrocomposite. Hot coextrusion of the AZ31–1.5 vol.%$Al_2O_3$/AA5052 macrocomposite billets produced

macrocomposite rods with AZ31–1.5 vol.%$Al_2O_3$ shell and AA5052 core (designated as AZ31–1.5 vol.%$Al_2O_3$/0.079 AA5052). The dimension of AA5052 core (AA5052 volume fraction) was fairly uniform along the length of the extruded rod. This can be attributed to mechanical interlocking between the AZ31-based shell and threaded AA5052 core.

## Microstructural characteristics

The average grain size obtained for the AZ31–1.5 vol.% $Al_2O_3$ shell of the macrocomposite was similar to that of monolithic AZ31 as shown in Table 1 and Fig. 2. The average grain size obtained for the AA5052 core of the macrocomposite was similar to that obtained from Hall-Williamson plots based on available XRD peaks corresponding to aluminum [20, 21, 23, 24]. In the macrocomposite, the grain size of the AZ31–1.5 vol.%$Al_2O_3$ shell was about one order of magnitude higher than that of the AA5052 core.

Including regions away from the AZ31–1.5 vol.%$Al_2O_3$–AA5052 interface: $Al_{12}Mg_{17}$ intermetallic particles were observed in monolithic AZ31 and the AZ31–1.5 vol.% $Al_2O_3$ shell of the macrocomposite as listed in Table 1 and shown in Fig. 2. The size and roundness ratio of $Al_{12}Mg_{17}$ intermetallic particles were lower in the AZ31–1.5 vol.% $Al_2O_3$ shell of the macrocomposite. Compared to $Al_{12}Mg_{17}$ intermetallic particles in the AZ31–1.5 vol.%$Al_2O_3$ shell of the macrocomposite, similar sized but less rounded $Al_{3.21}Si_{0.47}$ and $Al_mFe$ ($2.7 < m < 3.3$) intermetallic particles were observed in the AA5052 core of the macrocomposite.

$Al_2O_3$ nanoparticle reinforcement distribution in the AZ31–1.5 vol.%$Al_2O_3$ shell of the macrocomposite was reasonably uniform as shown in Fig. 2c, d. The $Al_2O_3$ nanoparticles were located at the grain boundary as well as within the grain.

Physical integrity of the AZ31–1.5 vol.%$Al_2O_3$–AA5052 macrointerface was found to be good based on (a) minimal presence of debonded regions and (b) evidence of significant diffusion of Mg and Al into each other as shown in Fig. 3. This was expected in accordance with their mutual solid-state solubility shown in the Al–Mg phase diagram [38]. It was also observed that intermetallic precipitation occurred at the interface.

AZ31 texture results are listed in Table 2 and shown in Fig. 4. In monolithic AZ31, the dominant textures in the transverse and longitudinal directions were (1 0 −1 0) and (1 0 −1 1) [and (0 0 0 2)], respectively. In AZ31–1.5 vol.%$Al_2O_3$/0.079 AA5052 macrocomposite, the dominant texture in the transverse and longitudinal directions were (1 0 −1 1) [and (1 0 −1 0)] and (1 0 −1 1), respectively.

**Table 1** Results of grain size, intermetallic particle characteristics, and microhardness of AZ31 and AZ31–1.5 vol.%$Al_2O_3$/0.079 AA5052 macrocomposite

| Material | Grain size[a] | | Intermetallic particle characteristics[b] | | | | Microhardness (HV) | | |
|---|---|---|---|---|---|---|---|---|---|
| | | | AZ31 monolith/shell | | AA5052 core | | AZ31 monolith/shell | AA5052 core | Macrointerface |
| | AZ31 monolith/shell (μm) | AA5052 core (nm) | Size (μm) | Roundness[c] ratio | Size (μm) | Roundness[c] ratio | | | |
| AZ31 | 4 ± 1 | – | 3.3 ± 1.1 | 1.9 | – | – | 64 ± 4 | – | – |
| AZ31–1.5 vol.%$Al_2O_3$/0.079 AA5052 | 4 ± 1 | 168 ± 34 | 1.2 ± 0.5 | 1.2 | 0.9 ± 0.3 | 1.6 | 85 ± 4 (+33) | 93 ± 4 (+45) | 110 ± 9 (+72) |

Values in brackets indicate %change with respect to corresponding result of AZ31

[a] Based on approximately 100 grains

[b] Based on approximately 100 particles

[c] Roundness measures the sharpness of a particle's edges and corners expressed by $(\text{perimeter})^2/4\pi(\text{area})$ [65]

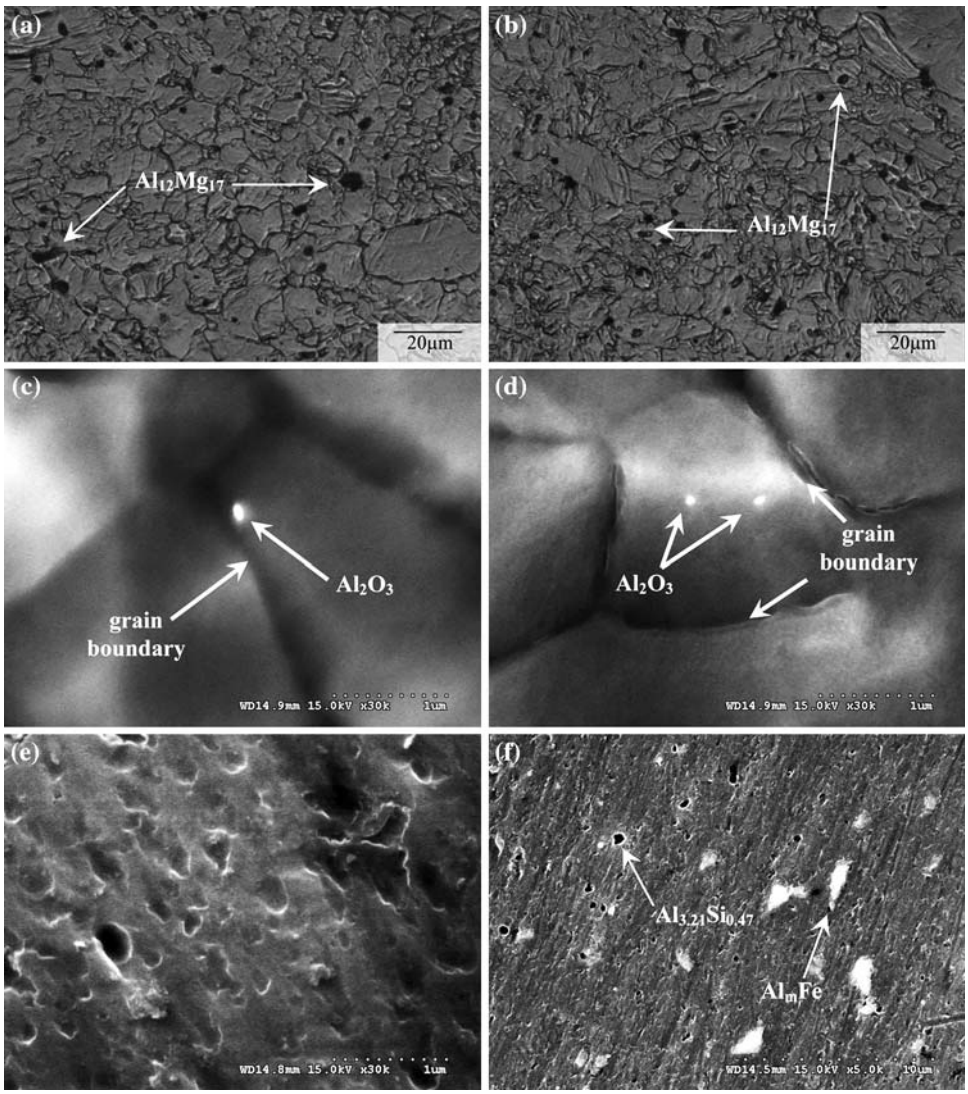


**Fig. 2** Representative micrographs showing (1) grain and intermetallic particle sizes in **a** monolithic AZ31 and **b** AZ31–1.5 vol.%$Al_2O_3$ nanocomposite shell of AZ31–1.5 vol.%$Al_2O_3$/0.079 AA5052 macrocomposite, (2) $Al_2O_3$ reinforcement distribution (location): **c** at the grain boundary and **d** within the grain in AZ31–1.5 vol.%$Al_2O_3$ nanocomposite shell of AZ31–1.5 vol.%$Al_2O_3$/0.079 AA5052 macrocomposite, (3) grain morphology in **e** AA5052 core of AZ31–1.5 vol.%$Al_2O_3$/0.079 AA5052 macrocomposite, and (4) intermetallic particle morphology in **f** AA5052 core of AZ31–1.5 vol.%$Al_2O_3$/0.079 AA5052 macrocomposite

## Hardness

The results of microhardness measurements are listed in Table 1. The AZ31–1.5 vol.%$Al_2O_3$ shell exhibited significantly higher average hardness than monolithic AZ31. In the macrocomposite, the AZ31–1.5 vol.%$Al_2O_3$ shell exhibited lower hardness than the AA5052 core. The AZ31–1.5 vol.%$Al_2O_3$–AA5052 interface exhibited significantly higher hardness compared to the AZ31–1.5 vol.%$Al_2O_3$ shell and AA5052 core.

## Tensile behavior

The overall results of ambient temperature tensile testing of the extruded materials are listed in Table 3 and shown in Fig. 5. The macrocomposite had higher stiffness, 0.2%TYS, UTS, failure strain, and work of fracture (WOF) than monolithic AZ31. The WOF was determined by computing the area under the tensile stress–strain curve. There was a step in the macrocomposite stress–strain curve. The top of the step corresponded to the shear fracture of the AZ31–1.5 vol.%$Al_2O_3$ shell, whereas the bottom of the step corresponded to the relatively fast transfer of load (i.e., mechanical shock) to the AA5052 core immediately after shear fracture of the AZ31–1.5 vol.%$Al_2O_3$ shell, after which the AA5052 core continued to deform until fracture. Fracture behavior of the AZ31–1.5 vol.%$Al_2O_3$ shell in the macrocomposite was ductile in shear (as that of monolithic AZ31) as shown in Fig. 6a, b. The AA5052 core in the macrocomposite exhibited ductile behavior in shear as shown in Fig. 6e. The tensile fractured surface of the macrocomposite showed a debonded AZ31–1.5 vol.%$Al_2O_3$–AA5052 macrointerface as shown in Fig. 6c, d.

## Compressive behavior

The overall results of ambient temperature compressive testing of the extruded materials are listed in Table 4 and

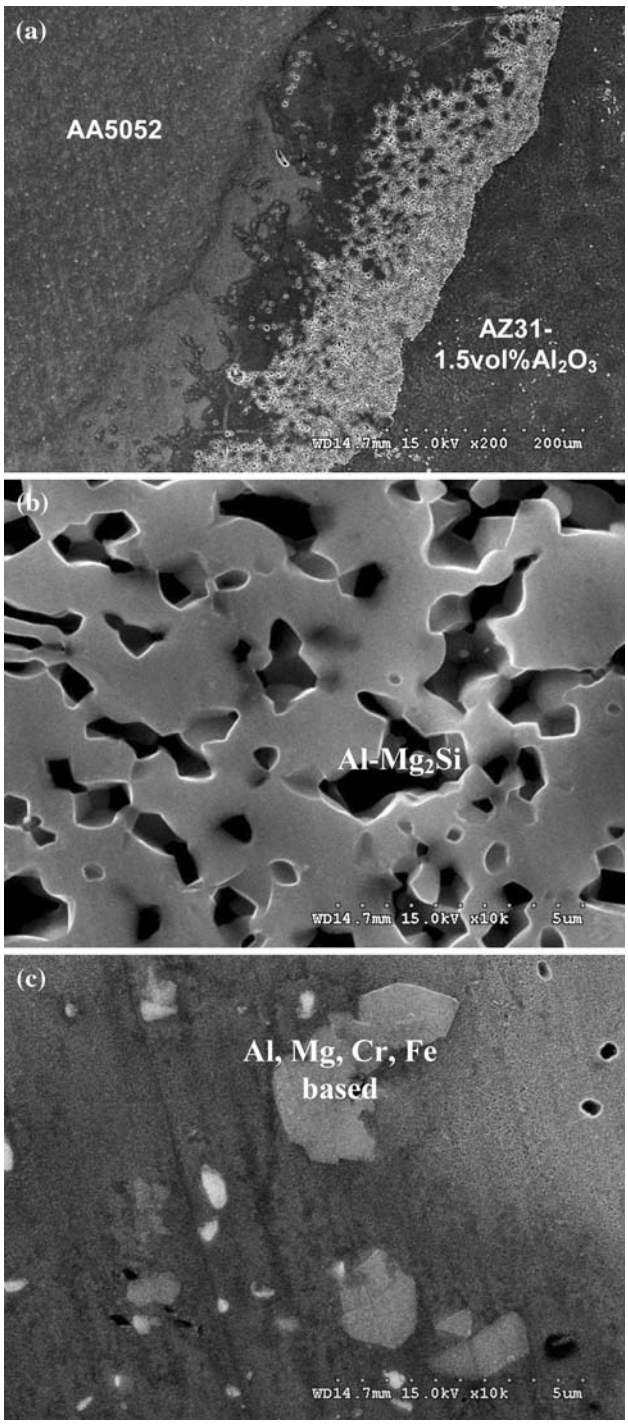


**Fig. 3** Representative micrographs showing (1) AZ31–1.5 vol.% $Al_2O_3$ shell–AA5052 core macrointerface in (**a**) and (2) intermetallic particles (precipitates) in **a** AZ31–1.5 vol.%$Al_2O_3$–AA5052 macrointerface (AZ31–1.5 vol.%$Al_2O_3$ side) and **b** AZ31–1.5 vol.%$Al_2O_3$–AA5052 macrointerface (AA5052 side)

shown in Fig. 5. The macrocomposite had higher 0.2%CYS, UCS, failure strain, and WOF than monolithic AZ31. There was a step in the macrocomposite stress–strain curve, similar to behavior in tension. The fractured surface of the AZ31–1.5 vol.%$Al_2O_3$ shell in the macrocomposite appeared smoother than that of monolithic AZ31 as shown in Fig. 7a, b. The AA5052 core in the macrocomposite exhibited ductile behavior in shear as shown in Fig. 7e. The compressive fractured surface of the macrocomposite showed an intact AZ31–1.5 vol.%$Al_2O_3$–AA5052 macrointerface as shown in Fig. 7c, d.

## Discussion

### Synthesis of AZ31 and AZ31–1.5 vol.%$Al_2O_3$/0.079 AA5052 materials

Synthesis of monolithic and macrocomposite material, the final form being extruded rods, was successfully accomplished with (a) no metal oxidation and (b) no detectable reaction between graphite crucible and melts. The inert atmosphere used during DMD was effective in preventing oxidation of the AZ31-based melt. No stable carbides of Mg or Al formed, due to reaction with graphite crucible. The 800 °C temperature used during top-pouring of AA5052 into machined AZ31–1.5 vol.%$Al_2O_3$ billets was sufficient to allow smooth filling of the cavity in the AZ31–1.5 vol.%$Al_2O_3$ billet.

### Microstructural characteristics

Microstructural characterization of extruded samples is discussed in terms of (a) grain size, (b) non-interface intermetallic particle characteristics (type, size, and roundness ratio), (c) $Al_2O_3$ nanoparticle reinforcement distribution, (d) interfacial integrity (debonding presence as well as intermetallic particle presence and type), and (e) AZ31 texture (in the longitudinal and transverse directions).

Metallography revealed that the grain size in the AZ31–1.5 vol.%$Al_2O_3$ shell of the macrocomposite was about one order of magnitude higher than that of the AA5052 core as shown in Table 1 and Fig. 2. This can be attributed to lower lattice diffusion and grain boundary diffusion rates in pure Al compared to pure Mg [20, 21, 23, 24, 39]. Diffusion rate calculations revealed that lattice diffusion rate and grain boundary diffusion rate in pure Al were 0.44 times and two orders lower than, respectively, that in pure Mg [20, 21, 23, 24, 39]. The similarity in grain size of monolithic AZ31 and AZ31–1.5 vol.%$Al_2O_3$ shell of the macrocomposite suggests similar diffusion profiles during hot extrusion in the nanocomposite shell compared to the corresponding monolithic alloy.

For intermetallic particles not located at the AZ31–1.5 vol.%$Al_2O_3$–AA5052 macrointerface, their characteristics are listed in Table 1 and shown in Fig. 2. Intermetallic particle size and roundness ratio were lower in the

**Table 2** Texture results of AZ31 and AZ31–1.5 vol.%$Al_2O_3$/0.079 AA5052 macrocomposite based on XRD

| Material | Section | Plane | Average $I/I_{max}$ [a] |
|---|---|---|---|
| AZ31 | T | 1 0 −1 0 prism | **1.00** |
| | | 0 0 0 2 basal | 0.16 |
| | | 1 0 −1 1 pyramidal | 0.81 |
| | L | 1 0 −1 0 prism | 0.27 |
| | | 0 0 0 2 basal | **0.93** |
| | | 1 0 −1 1 pyramidal | **1.00** |
| AZ31–1.5 vol.%$Al_2O_3$/0.079 AA5052 | T | 1 0 −1 0 prism | **0.92** |
| | | 0 0 0 2 basal | 0.75 |
| | | 1 0 −1 1 pyramidal | **1.00** |
| | L | 1 0 −1 0 prism | 0.32 |
| | | 0 0 0 2 basal | 0.50 |
| | | 1 0 −1 1 pyramidal | **1.00** |

*T* transverse, *L* longitudinal

[a] $I_{max}$ is XRD maximum intensity from either prism, basal, or pyramidal planes

Bold values indicate dominant textures in T and L sections

AZ31–1.5 vol.%$Al_2O_3$ shell of the macrocomposite, compared to that of monolithic AZ31. XRD analysis revealed the presence of $\beta$-$Al_{12}Mg_{17}$ phase [19]. The intermetallic particles were predominantly located at grain boundaries. The presence of $Al_2O_3$ nanoparticles assisted in breaking down the $\beta$-$Al_{12}Mg_{17}$ intermetallic phase.

The reasonably uniform distribution of $Al_2O_3$ nanoparticles as shown in Fig. 2c, d can be attributed to (a) minimal gravity-associated segregation due to judicious selection of stirring parameters [36], (b) good wetting of $Al_2O_3$ nanoparticles by the alloy matrix [40–42], (c) argon gas disintegration of metallic stream [43], and (d) dynamic deposition of composite slurry on substrate followed by hot extrusion. In the nanocomposite, no reaction products based on Mg and $Al_2O_3$ (such as MgO in this case [44]) having more than 2 vol.% were detected using XRD analysis.

In the macrocomposite, good physical integrity of the AZ31–1.5 vol.%$Al_2O_3$–AA5052 macrointerface based on the minimal presence of debonded regions, and presence of significant diffusion zones as shown in Fig. 3 can be attributed to (a) good wettability [33, 45, 46], (b) flow compatibility during hot coextrusion, and (c) ease of solid solution formation at the macrointerface between AZ31–1.5 vol.% $Al_2O_3$ shell and AA5052 core. For the interface (AZ31–1.5 vol.%$Al_2O_3$ side) of the macrocomposite, EDS point scan revealed the presence of Al–$Mg_2Si$ eutectic intermetallic particles (based on 5–6 at.%Al, 76–80 at.%Mg, and 20–24 at.%Si reading). This indicated significant diffusion of Al (from AA5052 core) into AZ31–1.5 vol.%$Al_2O_3$ shell resulting in Al-containing intermetallic particle precipitation. For the interface (AA5052 side) of the macrocomposite, EDS point scan revealed the presence of intermetallic particles consisting of Al, Mg, Cr, and Fe (based on 84–86 at.%Al, 16–18 at.%Mg, 11–13 at.%Cr, and 3–4 at.%Fe reading). This indicated significant diffusion of Mg (from AZ31–1.5 vol.%$Al_2O_3$ shell) into AA5052 core resulting in Mg-containing intermetallic particle precipitation. It was expected that the Mg content of the interface (AA5052 side) be significantly higher than the Al content of the interface (AZ31–1.5 vol.%$Al_2O_3$ side) based on (a) significantly higher solubility of Mg in Al than vice versa (18.6 at.%Mg in Al vs. 11.5 at.%Al in Mg, respectively [38]) and (b) grain size of AA5052 core being one order of magnitude less than that of AZ31–1.5 vol.%$Al_2O_3$ shell (see Table 1 and Fig. 2), when grain boundaries dominate in diffusion-controlled reactions at $T < 0.75T_m$, where $T$ is extrusion temperature and $T_m$ is melting point [47].

Unlike monolithic AZ31, AZ31–1.5 vol.%$Al_2O_3$/0.079 AA5052 macrocomposite did not exhibit (0 0 0 2) dominant texture in the longitudinal direction as listed in Table 2 and shown in Fig. 4. This difference in dominant texture can be attributed to the presence of (1) $Al_2O_3$ nanoparticles as well as smaller and more rounded intermetallic particles in the AZ31–1.5 vol.%$Al_2O_3$ shell and (2) AA5052 core having (a) lower mass specific heat capacity ($SHC_{mass}$) but higher density ($\rho$) and consequently about 1.3 times higher volume specific heat capacity ($SHC_{volume}$) compared to AZ31-based shell ($SHC_{mass}$ of AA5052 and AZ31 are 0.900 kJ/kg/K [48] and 1.040 kJ/kg/K [38], respectively, $\rho$ of AA5052 and AZ31 are 2680 kg/$m^3$ [48] and 1780 kg/$m^3$ [38], respectively, calculated $SHC_{volume}$ of AA5052 and AZ31 are 2412 kJ/$m^3$/K [48] and 1851 kJ/$m^3$/K [38], respectively, where $SHC_{volume} = \rho \times SHC_{mass}$) and (b) about 1.8 times higher thermal conductivity ($\kappa$) compared to AZ31-based shell ($\kappa$ of AA5052 and AZ31 are 137 W/m/K [48] and 76.9W/m/K [38], respectively). The implication here was that compared to (0 0 0 2) dominant texture formation in the longitudinal direction for monolithic AZ31, (1 0 −1 1) dominant texture formation [non-dominant (0 0 0 2) texture formation] in the longitudinal direction for AZ31–1.5 vol.%$Al_2O_3$/0.079 AA5052 macrocomposite occurred when (a) supplied quantity and (b) flow rate (based on $SHC_{volume}$ and $\kappa$, respectively) of heat from the AA5052 core to the AZ31-based shell in the transverse direction

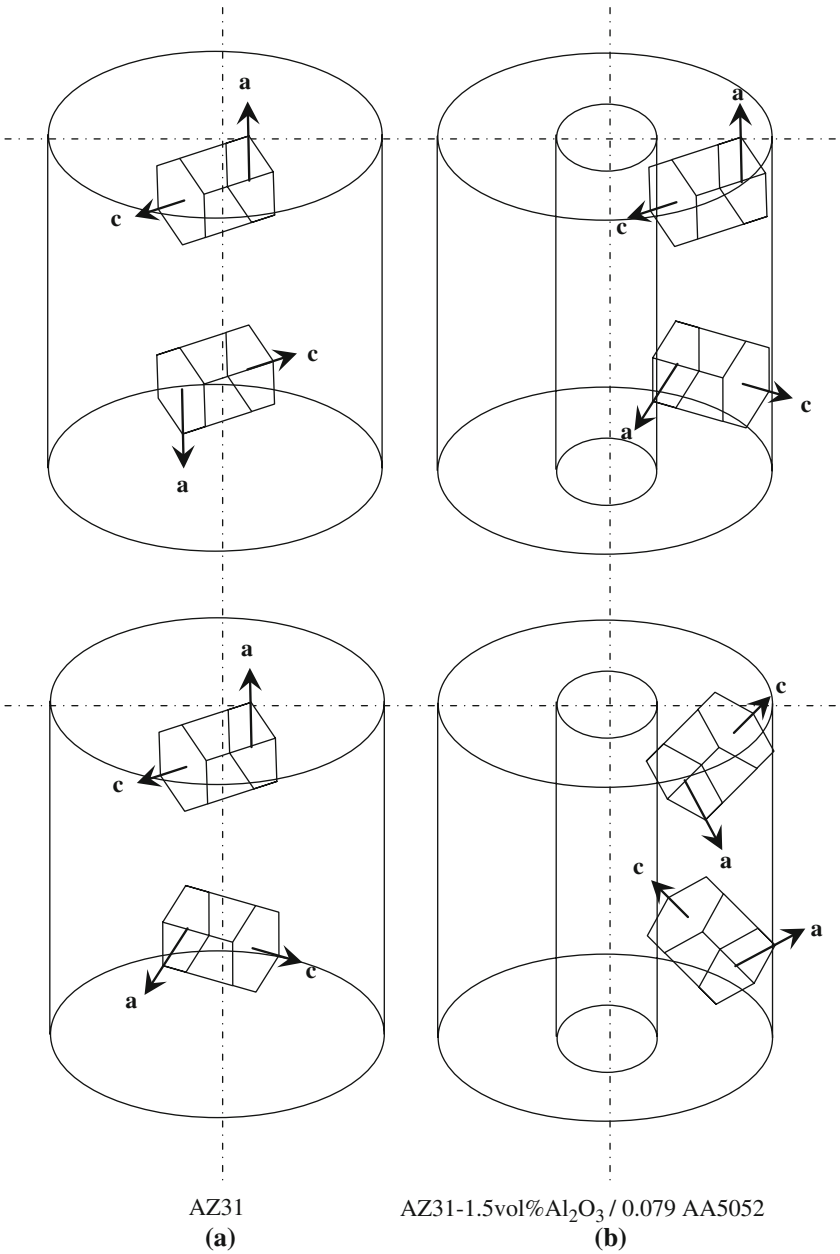


**Fig. 4** Schematic diagram showing textures of **a** AZ31 and **b** AZ31–1.5 vol.%$Al_2O_3$/0.079 AA5052, based on XRD. In each case, vertical axis is parallel to extrusion direction. Each cell is made up of two HCP units having one common (0 0 0 2) basal plane

**Table 3** Results of tensile testing of AZ31 and AZ31–1.5 vol.%$Al_2O_3$/0.079 AA5052 macrocomposite

| Material | *E* (GPa) | 0.2%TYS (MPa) | UTS (MPa) | Failure strain/elongation (%) | WOF (MJ/m$^3$)[a] |
|---|---|---|---|---|---|
| AZ31 | 44 ± 1 | 172 ± 15 | 263 ± 12 | 10.4 ± 3.9 | 26 ± 9 |
| AZ31–1.5 vol.%$Al_2O_3$/0.079 AA5052 | 61 ± 1 (+39) | 188 ± 10 (+9) | 312 ± 9 (+19) | 11.1 ± 0.4 (+7) | 33 ± 2 (+27) |

Values in brackets indicate %change with respect to corresponding result of AZ31

[a] Obtained from engineering stress–strain diagram using EXCEL software

(perpendicular to the extrusion direction) were each higher during hot coextrusion. At the same time, compared to monolithic AZ31, the AZ31–1.5 vol.%$Al_2O_3$ shell of the macrocomposite was located nearer the surface and therefore cooled faster. Particle presence and characteristics as well as annealing generally have been known to alter the texture in magnesium-based material [49, 50].

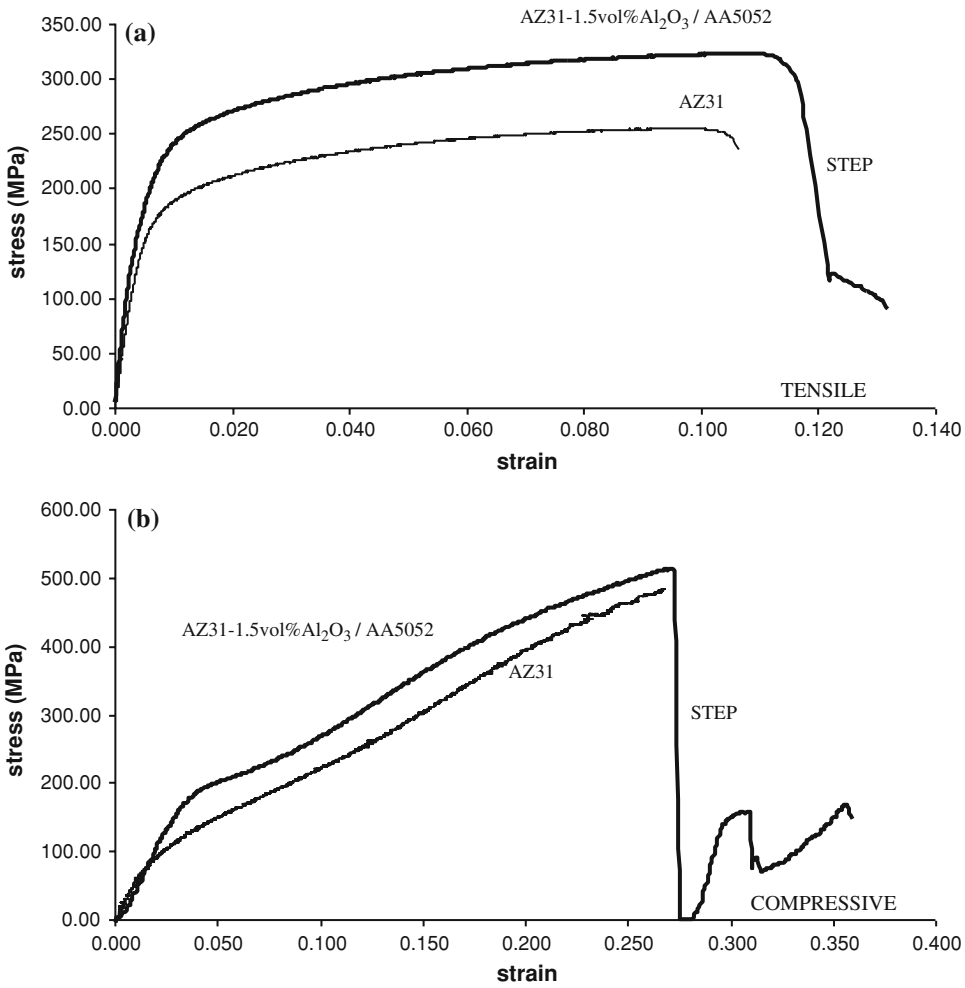


**Fig. 5** Representative **a** tensile and **b** compressive stress–strain curves of monolithic AZ31 and AZ31–1.5 vol.%$Al_2O_3$/0.079 AA5052 macrocomposite

## Hardness

A significant increase in microhardness by 33% was observed in the AZ31–1.5 vol.%$Al_2O_3$ shell of the AZ31–1.5 vol.%$Al_2O_3$/0.079 AA5052 macrocomposite when compared to monolithic AZ31 as listed in Table 1. This was consistent with earlier observations made on Mg/$Al_2O_3$, AZ31/$C_{60}$, and AZ31/MWCNT nanocomposites [5, 44, 51]. The increase in hardness of the AZ31–1.5 vol.%$Al_2O_3$ shell in this study can be attributed to (a) intermetallic particles of lower size and roundness ratio in the matrix, (b) reasonably uniform distribution of harder $Al_2O_3$ nanoparticles in the matrix, and (c) higher constraint to localized matrix deformation during indentation due to the presence of intermetallic particles (having lower size and roundness ratio) and nanoparticles [5, 6, 44]. In the macrocomposite, the significantly higher macrointerfacial microhardness (compared to that of AZ31–1.5 vol.%$Al_2O_3$ shell and AA5052 core) can be attributed to (a) strain localization [29], (b) solid solution formation between AZ31–1.5 vol.%$Al_2O_3$ and AA5052 with noticeable formation of intermetallics (see Fig. 3), and (c) accumulation of stress due to the difference in coefficient of thermal expansion (CTE) between Mg-based AZ31–1.5 vol.%$Al_2O_3$ and Al-based AA5052 (CTE of Mg is $28.90 \times 10^{-6}$/K [2], CTE of Al is $26.49 \times 10^{-6}$/K [2]).

## Stiffness

In the AZ31–1.5 vol.%$Al_2O_3$/0.079 AA5052 macrocomposite, the stiffness was 39% higher than that of monolithic AZ31 as listed in Table 3. This was due to the higher modulus of (a) AA5052 core, (b) $Al_2O_3$ ceramic nanoparticles in the AZ31–1.5 vol.%$Al_2O_3$ shell, and (c) AZ31–1.5 vol.%$Al_2O_3$–AA5052 macrointerface intermetallic particles. The integration between AZ31–1.5 vol.%$Al_2O_3$ and AA5052 was good, and the combined ability of (a)–(c) in increasing the stiffness of AZ31 was indicated [4, 24, 25]. The stiffness of the macrocomposite was 12% lower than that of AA5052 (69.3 GPa [48]).

## Strength

Compared to monolithic AZ31, AZ31–1.5 vol.%$Al_2O_3$/0.079 AA5052 macrocomposite had significantly higher

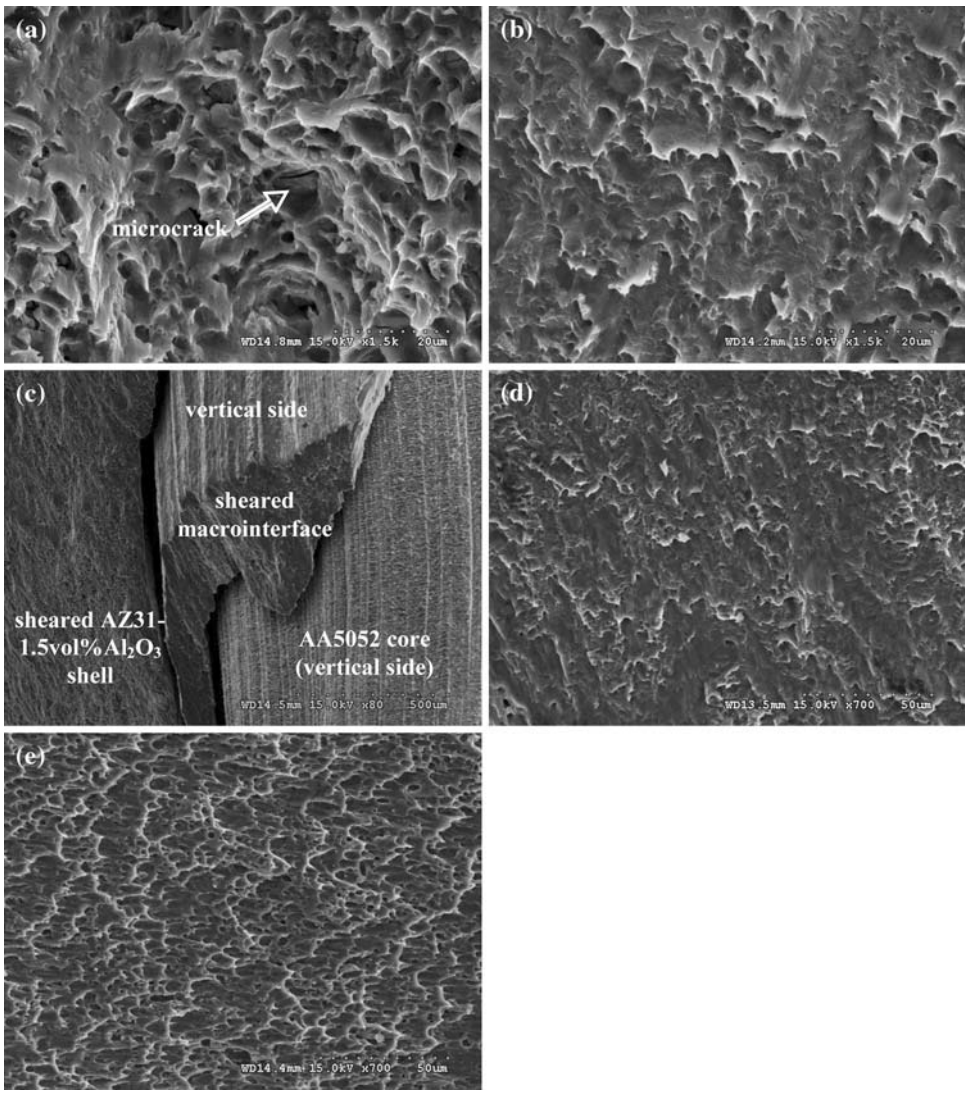


**Fig. 6** Representative FESEM micrographs showing tensile fracture surfaces of **a** monolithic AZ31, **b** AZ31–1.5 vol.%$Al_2O_3$ nanocomposite shell in AZ31–1.5 vol.%$Al_2O_3$/0.079 AA5052 macrocomposite, **c**, **d** AZ31–1.5 vol.%$Al_2O_3$–AA5052 macrointerface, and **e** AA5052 core in AZ31–1.5 vol.%$Al_2O_3$/0.079 AA5052 macrocomposite

**Table 4** Results of compressive testing of AZ31 and AZ31–1.5 vol%$Al_2O_3$/0.079 AA5052 macrocomposite

| Material | 0.2%CYS (MPa) | UCS (MPa) | Failure strain/ductility (%) | WOF (MJ/m$^3$)[a] |
|---|---|---|---|---|
| AZ31 | 93 ± 9 | 486 ± 4 | 19.7 ± 7.2 | 76 ± 14 |
| AZ31–1.5 vol.%$Al_2O_3$/0.079 AA5052 | 147 ± 6 (+58) | 504 ± 10 (+4) | 21.9 ± 3.6 (+11) | 115 ± 15 (+49) |

Values in brackets indicate %change with respect to corresponding result of AZ31

[a] Obtained from engineering stress–strain diagram using EXCEL software

0.2%TYS (9%) and UTS (19%) than monolithic AZ31 (see Table 3 and Fig. 5). This can be attributed to (a) reasonably uniform distribution of harder $Al_2O_3$ nanoparticles in the AZ31–1.5 vol.%$Al_2O_3$ shell (see Fig. 2), (b) AA5052 core exhibiting 45% higher microhardness than monolithic AZ31 (see Table 1), and (c) AZ31–1.5 vol.%$Al_2O_3$–AA5052 macrointerface being about 200 μm wide with noticeable precipitation of intermetallic particles (see Fig. 3). The associated strengthening mechanisms are (a) dislocation generation due to elastic modulus mismatch and CTE mismatch between the matrix and particle reinforcement [5, 6, 52, 53], (b) Orowan strengthening mechanism (inclusive of reduction in diameter of intermetallic particles in the AZ31–1.5 vol.%$Al_2O_3$ shell of the macrocomposite) [52–54], and (c) load transfer from matrix to particle reinforcement [5, 52]. This was the case despite (a) grain size of AZ31–1.5 vol.%$Al_2O_3$ shell in the macrocomposite being similar compared to that in monolithic AZ31 (see Fig. 2 also), and (b) inadequate AZ31–1.5 vol.%$Al_2O_3$–AA5052 macrointerfacial strength [matrix (shell)–reinforcement

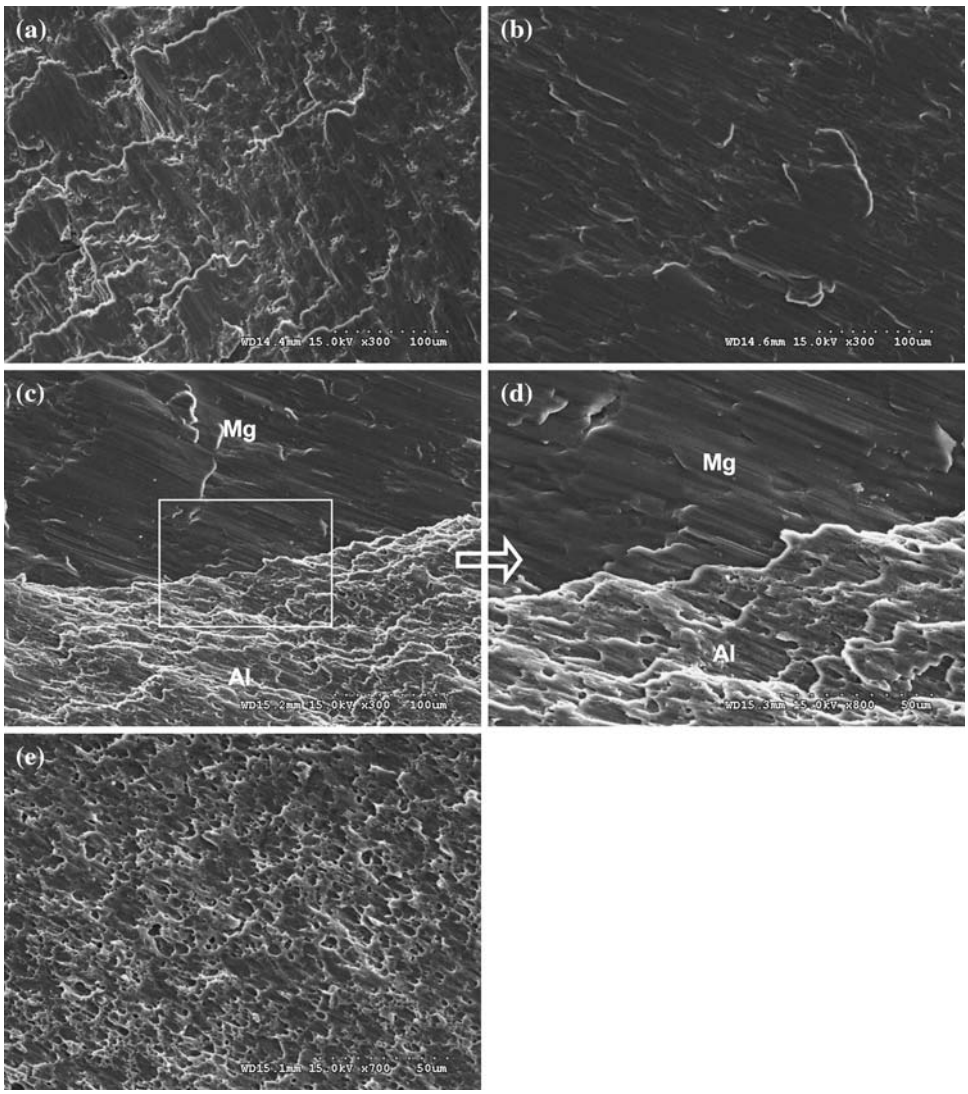


**Fig. 7** Representative FESEM micrographs showing compressive fracture surfaces of **a** monolithic AZ31, **b** AZ31–1.5 vol.%$Al_2O_3$ nanocomposite shell in AZ31–1.5 vol.%$Al_2O_3$/0.079 AA5052 macrocomposite, **c**, **d** AZ31–1.5 vol.%$Al_2O_3$–AA5052 macrointerface, and **e** AA5052 core in AZ31–1.5 vol.%$Al_2O_3$/0.079 AA5052 macrocomposite

(core) debonding of plastically sheared macrointerface shown in Fig. 6c, d]. This was also the case despite (c) (1 0 −1 1) dominant texture formation [non-dominant (0 0 0 2) texture formation] in the longitudinal and transverse directions of the AZ31–1.5 vol.%$Al_2O_3$/0.079 AA5052 macrocomposite unlike in monolithic AZ31 as listed in Table 2 and shown in Fig. 4. For this (1 0 −1 1) pyramidal plane texture, basal slip is made least difficult due to the low critical resolved shear stress (CRSS) for slip based on the 45° angle between the (0 0 0 2) basal plane and the vertical axis as shown in Fig. 4 [54, 55]. In similar comparison of compressive strength, 0.2%CYS and UCS of AZ31–1.5 vol.%$Al_2O_3$/0.079 AA5052 macrocomposite were higher by 58 and 4%, respectively, compared to monolithic AZ31 (see Table 4 and Fig. 5). The stress detected at much of the given strain was higher for AZ31–1.5 vol.%$Al_2O_3$/0.079 AA5052 macrocomposite compared to monolithic AZ31 as shown in Fig. 5b. The role of the AZ31–1.5 vol.%$Al_2O_3$–AA5052 macrointerface during deformation of the macrocomposite was to transfer stress adequately between the AA5052 core reinforcement and AZ31–1.5 vol.%$Al_2O_3$ shell matrix. In compression, the macrointerface performed this role perfectly based on its intact nature after fracture as shown in Fig. 7.

In monolithic AZ31, 0.2%TYS was about 1.8 times the 0.2%CYS. This can be attributed generally to (a) half the strain rate used (less strain hardening) in compressive testing compared to tensile testing and (b) $\{1\,0\,1\,-2\}\,\langle 1\,0\,1\,-1\rangle$-type twinning being more easily activated along the *c*-axis (of the HCP unit cell in Fig. 4) in tension than in compression along the *c*-axis [56, 57]. With the *c*-axis of the HCP unit cell oriented 90° to the force axis (extrusion direction) in this case, $\{1\,0\,1\,-2\}\,\langle 1\,0\,1\,-1\rangle$-type twinning was less easily activated in compression along the *c*-axis, during tensile testing (Poisson effect). In the AZ31–1.5 vol.%$Al_2O_3$/0.079 AA5052 macrocomposite, 0.2%TYS was only about 1.3

times the 0.2%CYS. Here, the TYS/CYS anisotropy was significantly reduced despite half the strain rate used (less strain hardening) in compressive testing compared to tensile testing. This can be similarly attributed to (a) $\{1\ 0\ 1\ -2\}\langle 1\ 0\ 1\ -1\rangle$-type twinning being activated along the *c*-axis of the HCP unit cell in Fig. 4 with comparatively similar ease in both tension and compression along the *c*-axis, based on the 45° angle between the *c*-axis and the vertical axis [56, 57] and (b) generally non-preferential slip system activation in the relatively isotropic FCC unit cell of AA5052 aluminum alloy.

## Failure strain

The tensile and compressive failure strains of monolithic AZ31 and AZ31–1.5 vol.%$Al_2O_3$/0.079 AA5052 macrocomposite are listed in Tables 3 and 4 (and shown in Fig. 5a, b), respectively. Compared to monolithic AZ31, average tensile and compressive failure strains were increased by 7 and 11%, respectively, in the macrocomposite. This was despite the noticeable formation of intermetallic particles at the AZ31–1.5 vol.%$Al_2O_3$–AA5052 macrointerface as shown in Fig. 3. This increase in failure strain can be attributed to (a) presence and reasonably uniform distribution of $Al_2O_3$ nanoparticles in the AZ31–1.5 vol.%$Al_2O_3$ shell of the macrocomposite (see Fig. 2) [44, 58], and (b) reduction in size and roundness ratio of intermetallic particles in the AZ31–1.5 vol.%$Al_2O_3$ shell of the macrocomposite (see Table 1 and Fig. 2) [59]. This increase in failure strain can also be attributed to (c) (1 0 −1 1) dominant texture formation [non-dominant (0 0 0 2) texture formation] in the longitudinal and transverse directions of the AZ31–1.5 vol.%$Al_2O_3$ shell of the macrocomposite unlike in monolithic AZ31 as listed in Table 2 and shown in Fig. 4. In the case of reasonably uniform distribution of ceramic nanoparticles, it has been shown in previous studies that the nanoparticles provide sites where cleavage cracks are opened ahead of the advancing crack front. This (1) dissipates the stress concentration which would otherwise exist at the crack front and (2) alters the local effective stress state from plane strain to plane stress in the neighborhood of crack tip [44, 58]. In the case of reduction in size and roundness ratio of intermetallic particles, roundness is a measure of the sharpness of a particle's edges and corners. Breakdown of the intermetallic particles located at grain boundaries and the change in their distribution from a predominantly aggregated type to dispersed type as also observed in this study can assist in improving ductility [59]. In the case of (1 0 −1 1) dominant texture formation [non-dominant (0 0 0 2) texture formation] in the longitudinal and transverse directions, basal slip is made least difficult due to the low CRSS for slip based on the 45° angle between the (0 0 0 2) basal plane and the vertical axis [54, 55].

Tensile fracture behavior of monolithic AZ31, AZ31–1.5 vol.%$Al_2O_3$ shell, and AA5052 core (of the macrocomposite) was ductile in shear as shown in Fig. 6. The involvement of shear during deformation and fracture can be attributed to shear localization around (a) intermetallic particles and (b) voids in the deformed matrix surrounding the intermetallic particles, in alloys [60, 61]. However, the tensile fractured surface of AZ31–1.5 vol.%$Al_2O_3$ shell had (a) higher occurrence of smaller dimple-like features and (b) absence of microcracks, compared to that of monolithic AZ31. The tensile cavitation resistance was lower and the microcrack formation resistance was higher in the AZ31–1.5 vol.%$Al_2O_3$ shell compared to monolithic AZ31. For the macrocomposite, compressive fracture behavior of the AZ31–1.5 vol.%$Al_2O_3$ shell based on viscous flow [62] was relatively more ductile (smoother fracture surface exhibited) compared to monolithic AZ31 as shown in Fig. 7. This relatively more ductile compressive fracture behavior can be attributed to increase in shear band spacing [62, 63].

## Work of fracture

The tensile and compressive WOF of monolithic AZ31 and AZ31–1.5 vol.%$Al_2O_3$/0.079 AA5052 macrocomposite are listed in Tables 3 and 4 (and illustrated in Fig. 5a, b), respectively. WOF quantified the ability of the material to absorb energy up to fracture under load [64]. Compared to monolithic AZ31, tensile WOF and compressive WOF were enhanced by 27 and 49%, respectively, in AZ31–1.5 vol.%$Al_2O_3$/0.079 AA5052 macrocomposite.

Finally, compared to monolithic AZ31, the significantly higher stiffness, strength, and WOF exhibited by AZ31–1.5 vol.%$Al_2O_3$/0.079 AA5052 macrocomposite as shown in Tables 3 and 4 show its potential to be used in stiffness and strength-based design as well as damage-tolerant design, respectively.

## Conclusions

1. AZ31–1.5 vol.%$Al_2O_3$/AA5052 macrocomposite can be successfully synthesized using solidification processing coupled with hot coextrusion.
2. Compared to monolithic AZ31, stiffness of AZ31–1.5 vol.%$Al_2O_3$/0.079 AA5052 macrocomposite was enhanced. This can be attributed to the higher elastic modulus of (a) AA5052 core, (b) $Al_2O_3$ ceramic nanoparticles in the AZ31–1.5 vol.%$Al_2O_3$ shell, and (c) AZ31–1.5 vol.%$Al_2O_3$–AA5052 macrointerface intermetallic particles.

3. Compared to monolithic AZ31, tensile and compressive strength of AZ31–1.5 vol.%$Al_2O_3$/0.079 AA5052 macrocomposite were enhanced. This can be attributed to (a) reasonably uniform distribution of harder $Al_2O_3$ nanoparticles in the AZ31–1.5 vol.%$Al_2O_3$ shell, (b) AA5052 core exhibiting 45% higher microhardness than monolithic AZ31, and (c) AZ31–1.5 vol.%$Al_2O_3$–AA5052 macrointerface being about 200 μm wide with noticeable precipitation of intermetallic particles.
4. Compared to monolithic AZ31, tensile and compressive average failure strain of AZ31–1.5 vol.%$Al_2O_3$/0.079 AA5052 macrocomposite were increased. This can be attributed to (a) presence and reasonably uniform distribution of $Al_2O_3$ nanoparticles, (b) reduction in size and roundness ratio of intermetallic particles, and (c) (1 0 −1 1) dominant texture formation [non-dominant (0 0 0 2) texture formation] in the longitudinal and transverse directions, in the AZ31–1.5 vol.%$Al_2O_3$ shell of the macrocomposite.
5. Compared to monolithic AZ31, tensile and compressive WOF of AZ31–1.5 vol.%$Al_2O_3$/0.079 AA5052 macrocomposite were enhanced. This can be attributed to the combined effect of increased tensile and compressive strengths and increased average failure strain of AZ31–1.5 vol.%$Al_2O_3$/0.079 AA5052 macrocomposite.

**Acknowledgements** The authors acknowledge NUS research scholarship for PhD candidature of M. Paramsothy for supporting this research.

## References


1. Clyne TW, Withers PJ (1993) An introduction to metal matrix composites. Cambridge University Press, Cambridge
2. Brandes EA, Brook GB (eds) (1998) Smithells light metals handbook. Reed Educational and Professional Publishing Ltd, Chicago, IL, pp 5, 40–54
3. Ferkel H, Mordike BL (2001) Mater Sci Eng A 298:193
4. Hassan SF, Gupta M (2006) Compos Struct 72:19
5. Hassan SF, Gupta M (2006) J Mater Sci 41:2229. doi:10.1007/s10853-006-7178-3
6. Goh CS, Wei J, Lee LC, Gupta M (2006) Nanotechnology 17:7
7. Hassan SF, Gupta M (2002) J Alloys Compd 345:246
8. Perez P, Garces G, Adeva P (2004) Compos Sci Technol 64:145
9. Wong WLE, Gupta M (2005) Adv Eng Mater 7:250
10. Hassan SF, Gupta M (2002) J Alloys Compd 335:L10
11. Huard G, Angers R, Krishnadev MR, Tremblay R, Dube D (1999) Can Metall Q 38:193
12. Morisada Y, Fujii H, Nagaoka T, Fukusumi M (2006) Mater Sci Eng A 433:50
13. Morisada Y, Fujii H, Nagaoka T, Fukusumi M (2006) Scr Mater 55:1067
14. Morisada Y, Fujii H, Nagaoka T, Fukusumi M (2006) Mater Sci Eng A 419:344
15. Ding WB, Jiang HY, Zeng XQ, Li DH, Yao SS (2007) Appl Surf Sci 253:3877
16. Ding W, Jiang H, Zeng X, Li D, Yao S (2007) Mater Lett 61:496
17. Wenbin D, Haiyan J, Xiaoqin Z, Dehui L, Shoushan Y (2007) J Alloys Compd 429:233
18. Mizuuchi K, Inoue K, Hamada K, Sugioka M, Itami M, Fukusumi M, Kawahara M (2004) Mater Sci Eng A 367:343
19. Nguyen QB, Gupta M (2007) J Alloys Compd 459:244
20. Paramsothy M, Srikanth N, Gupta M (2008) J Compos Mater. doi:10.1177/0021998308098369
21. Paramsothy M, Srikanth N, Gupta M (2008) J Alloys Compd 461:200
22. Paramsothy M, Srikanth N, Gupta M (2008) J Compos Mater 42(13):1297
23. Paramsothy M, Srikanth N, Hassan SF, Gupta M (2008) Mater Sci Eng A 494:436
24. Paramsothy M, Hassan SF, Srikanth N, Gupta M (2008) J Phys D 41:175402
25. Abbasi M, Taheri AK, Salehi MT (2001) J Alloys Compd 319:233
26. Dyja H, Mroz S, Stradomski Z (2003) Metalurgija 42:185
27. Dyja H, Mroz S, Milenin A (2004) J Mater Process Technol 153–154:100
28. Krishna BV, Venugopal P, Rao KP (2005) Mater Sci Eng A 407:77
29. Krishna BV, Venugopal P, Rao KP (2004) Mater Sci Eng A 386:301
30. Jiang F, Zhao K, Sun J (2003) Int J Press Vessels Piping 80:129
31. Manesh HD, Taheri AK (2003) J Alloys Compd 361:138
32. Kapinski S (1996) J Mater Process Technol 60:197
33. Marukovich EI, Branovitsky AM, Na Y-S, Lee J-H, Choi K-Y (2006) Mater Des 27(10):1016
34. An J, Liu YB, Zhang MZ, Yang B (2002) J Mater Process Technol 120:30
35. Mamalis AG, Szalay A, Vaxevanidis NM, Pantelis DI (1994) Mater Sci Eng A 188:267
36. Tham LM, Gupta M, Cheng L (1999) Mater Sci Technol 15:1139
37. Gupta M, Lai MO, Lim SC (1997) J Alloys Compd 260:250
38. Avedesian MM, Baker H (1999) ASM specialty handbook: magnesium and magnesium alloys. ASM International, Ohio, pp 4–6, 10, 11, 28, 37, 258, 259, 274
39. Frost HJ, Ashby MF (1982) Deformation-mechanism maps. The plasticity and creep of metals and ceramics. Pergamon Press Ltd, Oxford, pp 21, 44
40. Han BQ, Dunand DC (2000) Mater Sci Eng A 277:297
41. Eustathopoulos N, Nicholas MG, Drevet B (1999) Wettability at high temperatures, vol 3. Pergamon Materials SeriesPergamon, New York
42. Gilchrist JD (1989) Extraction metallurgy, 3rd edn. Pergamon Press, New York
43. Gupta M, Lai MO, Soo CY (1996) Mater Sci Eng A 210:114
44. Hassan SF, Gupta M (2006) J Alloys Compd 419:84
45. Molina JM, Voytovych R, Louis E, Eustathopoulos N (2007) Int J Adhes Adhes 27:394
46. Shen P, Nose M, Fujii H, Nogi K (2006) Thin Solid Films 515(4):2009
47. Cahn RW (1970) Physical metallurgy. North-Holland Publishing Company, Amsterdam, pp 397–399
48. The ASM International Handbook Committee (1990) Metals handbook, vol 2, 10th edn. ASM International, Ohio, pp 101–102
49. Mackenzie LWF, Davis B, Humphreys FJ, Lorimer GW (2007) Mater Sci Technol 23(10):1173
50. Jager A, Lukac P, Gartnerova V, Haloda J, Dopita M (2006) Mater Sci Eng A 432:20
51. Hassan SF, Gupta M (2005) Metall Mater Trans A 36(8):2253
52. Szaraz Z, Trojanova Z, Cabbibo M, Evangelista E (2007) Mater Sci Eng A 462:225
53. Dai LH, Ling Z, Bai YL (2001) Compos Sci Technol 61:1057

54. Hull D, Bacon DJ (2002) Introduction to dislocations, 4th edn. Butterworth-Heinemann, Oxford, pp 43, 231
55. Mukai T, Yamanoi M, Watanabe H, Higashi K (2001) Scr Mater 45:89
56. Laser T, Hartig C, Nurnberg MR, Letzig D, Bormann R (2008) Acta Mater 56:2791
57. Bohlen J, Yi SB, Swiostek J, Letzig D, Brokmeier HG, Kainer KU (2005) Scr Mater 53:259
58. Hassan SF, Gupta M (2007) J Alloys Compd 429:176
59. Dieter GE (1988) Mechanical metallurgy, SI metric edn. McGraw-Hill Book Company, London
60. Spencer K, Corbin SF, Lloyd DJ (2002) Mater Sci Eng A 325:394
61. Hu XH, Jain M, Wilkinson DS, Mishra RK (2008) Acta Mater. doi:10.1016/j.actamat.2008.02.048
62. Batra RC, Wei ZG (2007) Int J Impact Eng 34:448
63. Wang TS, Hou RJ, Lv B, Zhang M, Zhang FC (2007) Mater Sci Eng A 465:68
64. Reed-Hill RE (1964) Physical metallurgy principles, 2nd edn. D Van Nostrand Company, New York, pp 192, 267, 725
65. Ganesh VV, Gupta M (2000) Mater Res Bull 35:2275